

## Excitation parameters optimized for coherent anti-Stokes Raman scattering imaging of myelinated tissue

Craig Brideau  
Kelvin W. C. Poon  
Pina Colarusso  
Peter K. Stys

# Excitation parameters optimized for coherent anti-Stokes Raman scattering imaging of myelinated tissue

Craig Brideau,<sup>a,\*</sup> Kelvin W. C. Poon,<sup>a</sup> Pina Colarusso,<sup>b,c</sup> and Peter K. Stys<sup>a</sup>

<sup>a</sup>University of Calgary, Hotchkiss Brain Institute, Cumming School of Medicine, Department of Clinical Neurosciences, Calgary, Alberta, Canada

<sup>b</sup>University of Calgary, Department of Physiology and Pharmacology, Calgary, Alberta, Canada

<sup>c</sup>University of Calgary, Snyder Institute for Chronic Diseases, Cumming School of Medicine, Calgary, Alberta, Canada

**Abstract.** Coherent anti-Stokes Raman scattering (CARS) generates a strong label-free signal in the long wavenumber C—H stretching region. Lipid-rich myelinated tissues, such as brain and spinal cord, would appear to be ideal subjects for imaging with CARS laser-scanning microscopy. However, the highly ordered, biochemically complex, and highly scattering nature of such tissues complicate the use of the technique. A CARS microscopy approach is presented that overcomes the challenges of imaging myelinated tissue to achieve chemically and orientationally sensitive high-resolution images. © The Authors. Published by SPIE under a Creative Commons Attribution 4.0 Unported License. Distribution or reproduction of this work in whole or in part requires full attribution of the original publication, including its DOI. [DOI: 10.1117/1.JBO.24.4.046502]

Keywords: nonlinear optics; coherent anti-Stokes Raman scattering; myelin; polarization; dispersion; Raman scattering.

Paper 190012R received Jan. 11, 2019; accepted for publication Mar. 25, 2019; published online Apr. 21, 2019.

## 1 Introduction

Coherent anti-Stokes Raman scattering (CARS) is a label-free nonlinear imaging technique that probes vibrational resonances in molecular bonds to generate contrast. CARS signal generation is strongly dependent on the orientation and concentration of vibrational modes within the sample. CARS can, therefore, be used to probe the nanostructural orientation of vibrational bonds within ordered samples.<sup>1–3</sup>

CARS requires two laser sources, termed “pump” ( $\omega_p$ ) and “Stokes” ( $\omega_s$ ), which are tuned such that the energy difference between the frequencies of the two beams matches the potential energy in the vibrational resonance of a molecule. A photon from a third beam, the “probe” ( $\omega_{pr}$ ), then interrogates the excited vibrational mode, generating a blueshifted photon, the “anti-Stokes” ( $\omega_{as}$ ). In two-beam CARS configurations,  $\omega_{pr} = \omega_p$  and the pump also act as the probe source.<sup>4–6</sup>

In Raman spectroscopy nomenclature, the “C—H region” contains strong CH<sub>2</sub> and CH<sub>3</sub> stretching modes ranging from ~2800 to 3100 cm<sup>-1</sup>. Lipids typically contain long acyl chains with many C—H bonds in each molecule, providing a high concentration of Raman-active oscillators. The vibrational resonance of a hydrocarbon chain is primarily due to the motion of the hydrogen atoms, as they are much lighter than carbon. The relatively stationary nature of the carbon limits vibrational coupling to any other adjacent modes. This leads to a large frequency mismatch with other modes that, combined with long CH<sub>2</sub> acyl chains, creates a very distinct C—H stretch in lipids. The CH<sub>2</sub> symmetric and asymmetric vibrational modes are particularly abundant in the long acyl chains of biological cell membranes, and especially in myelin that consists of multiple compacted wraps of extended glial cell membranes.<sup>7–9</sup>

Myelin is the insulating sheath surrounding myelinated axons and is composed of ~30% protein and ~70% lipid by dry weight.<sup>10</sup> Its structure consists of sequential layers of

complex bilayer membrane wrapped around a cylindrical axon. Hundreds of different lipid moieties are contained in the membrane, such as sphingomyelins, phospholipids, and glycosphingolipids;<sup>11</sup> the carbon backbone is oriented perpendicularly to the surface of the axon, leading to a radial orientation around the cylinder of the enclosed axon.<sup>12</sup>

Both the order and tight packing of the membrane layers create a dense, highly directional distribution of C—H bonds. As will be shown, the CH<sub>2</sub> symmetric vibration is the most sensitive to the polarization orientation of the excitation. Aligning the polarization of the  $\omega_p$  and  $\omega_s$  beams parallel to the membrane layers maximizes contrast between the ordered CH<sub>2</sub> symmetric stretch and any isotropic background signal.

This paper describes a CARS system optimized to exploit the directional nature of the CH<sub>2</sub> symmetric stretch in myelin lipids. An automated polarization control system allowing orientationally sensitive interrogation of C—H bonds is presented. In combination with this directional sensitivity, a spectral focusing prism set providing chemical sensitivity comparable to conventional Raman is described. Finally, the application of combined polarization and orientationally specific sample excitation for myelin sample imaging is presented. Together, these capabilities provide a unique ability to interrogate the nanostructure and lipid chemistry of myelin in health and disease.

## 2 Theory

CARS imaging requires precise control over the spatial and temporal overlap of multiple laser pulses. Additional complexity is required for polarization control and vibrational selectivity to achieve the best contrast between myelin and background signals.

### 2.1 Coherent Anti-Stokes Raman Scattering Vibrational Selectivity

In many configurations,  $\omega_p$  and  $\omega_{pr}$  are both provided by a single-laser pulsed source at the same wavelength (degenerate CARS). Combining the  $\omega_p$  and  $\omega_{pr}$  into one beam is

\*Address all correspondence to Craig Brideau, E-mail: [cbrideau@ucalgary.ca](mailto:cbrideau@ucalgary.ca)

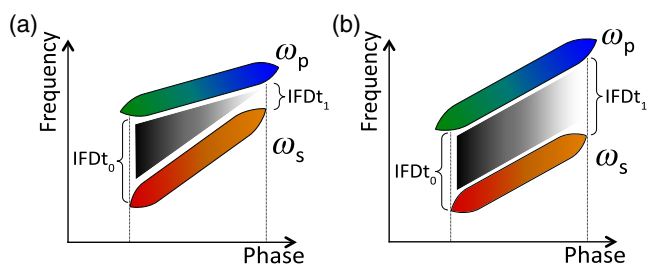


**Fig. 1** Representative plots of phase and frequency for two broadband sources with (a) unmatched chirp ( $IFD_{t_0} \neq IFD_{t_1}$ ) and (b) matched chirp ( $IFD_{t_0} = IFD_{t_1}$ ). Shaded area highlights frequency difference between the two sources at any instant.

advantageous due to the complexity of manipulating separate beams involved in the CARS process. For this treatment,  $\omega_p$  and  $\omega_{pr}$  will be identical and simply referred to as  $\omega_p$ .

The frequency difference between  $\omega_p$  and  $\omega_s$  should be matched to the resonant frequency of the targeted molecular vibration. Each vibrational regime of a molecular bond will have a finite bandwidth associated with interactions of the bond with the rest of the molecule and the environment. For the lipid region under physiological conditions, the bandwidth of the various C–H modes is on the order of 10 to 30  $\text{cm}^{-1}$ .<sup>13</sup> The bandwidth of excitation should be matched to the bandwidth of the vibrational mode for optimal excitation.<sup>9,14</sup> This is achieved either by having spectrally narrow lasers or spectrally focusing chromatically broad lasers to maintain a constant instantaneous frequency difference (IFD) over the duration of the pulses. A narrow IFD selects for a specific vibrational mode, thus directing energy more efficiently into exciting the sample rather than competing background effects or closely related vibrations.

The IFD between two broadband sources can be maintained by temporally chirping the two pulses such that the rate of frequency variation in time is held constant and identical between the two pulses. Chirping can be controlled by passage of the pulses through specific lengths of glass, or the use of grating or prism assemblies. These methods allow adjustment of the phase of the various wavelength components of each pulse and must be balanced so that the frequency change per unit time (or phase) is identical for both pulses (matched chirp) (Fig. 1).

Propagation through glass allows controlled amounts of dispersion to be applied to broadband pulses and is a geometry that is less alignment sensitive than grating or prism-based designs. The Sellmeier equation<sup>6</sup> describes the index of refraction variation with respect to wavelength for various types of glass while the derivatives predict the second- and higher-order dispersion properties. In this case, a material with high second-order dispersion is desirable as this term imparts linear chirp. Third- and higher-order terms in the dispersion equation create more complex phase distributions that negatively impact the IFD.

## 2.2 Ordered Lipid Polarization Effects

The wraps of cell membrane comprising myelin are phospholipid bilayers with some embedded proteins. While many types of lipid are present, most feature some variation of a polar head group with nonpolar tails composed of C–H bonds. The head group is hydrophilic, whereas the tail is hydrophobic. When surrounded by water, the molecules assemble into layers with the hydrophobic tails pointing inward away from the water. This leads to a sandwich of hydrophilic (polar) head groups top and bottom interacting with water, whereas the hydrophobic (nonpolar) tails point inward between the head group layers.<sup>7</sup>

The alignment of the nonpolar C–H chains within the bilayer creates a strong directional preference for the various resonances.  $\text{CH}_2$  bonds form the majority of the backbone with the hydrogen atoms extending outward roughly perpendicular to the direction of the carbon chain. The  $\text{CH}_2$  bond vibrations exhibit strongest CARS resonance when aligned with the exciting field, meaning the directional preference of the overall bilayer structure is parallel to the membrane (Fig. 2). This condition requires the electric fields of both  $\omega_p$  and  $\omega_s$  pulses to be aligned with the membrane structure of the sample for optimal CARS signal generation.

In practice, a given sample will have these membranes lying in many different directions. To probe a sample with a variety of orientations, it is necessary to rotate either the sample or the polarization of the incident lasers. Rotating a sample smoothly under a microscopic field of view is mechanically challenging as the center of rotation must correspond to the center of the field of view. Creating pure rotation with no offset in other

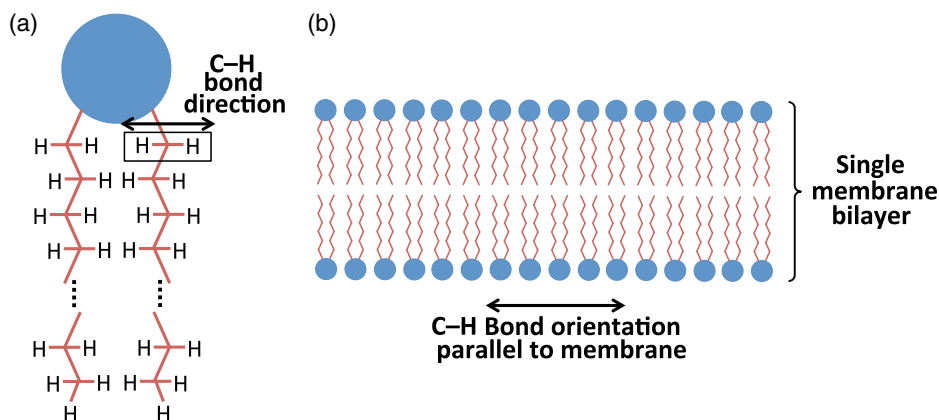


**Fig. 2** (a) Schematic representation of a lipid molecule illustrating orientation of hydrogen bonds relative to the carbon backbone of the hydrophobic tail. Large circle represents the hydrophilic polar head group. (b) Illustration of an ideal membrane bilayer highlighting the orientation of C–H bonds parallel to the membrane surface.

dimensions is impractical for a microscope stage. Conversely, manipulating the polarization of the lasers can be achieved with waveplate optical elements inserted into the beam. The technical details of this approach are discussed in Sec. 3.

### 2.3 Light Scattering

Myelinated tissue strongly scatters light in both the visible and NIR wavelength ranges.<sup>8</sup> The white coloration of myelinated “white matter” is due to Mie scattering<sup>8</sup> of visible light from the tissue. As  $\omega_p$  and  $\omega_s$  propagate through the tissue, scattering and absorption events cause an exponential reduction in intensity<sup>9</sup> and a broadening of phase. Collision events between the sample and the photons comprising the incident beams impart a delay as different photons scatter along paths of varying length.<sup>9</sup>

To achieve sufficient power density at the sample, it is necessary to increase the quantity of photons reaching the focal point. This can be achieved by increasing the average power of the incident beams, but this leads to undesirable sample heating. Due to the nonlinear nature of the CARS process, peak pulse energy rather than average power is the principal driver of signal. Increasing peak power while reducing the repetition rate increases signal while maintaining the same average power.

Finally, careful selection of the center wavelengths of  $\omega_p$  and  $\omega_s$  can take advantage of the optical absorption properties of lipids. The Raman CH lipid region requires particular wavenumber spacing between  $\omega_p$  and  $\omega_s$ , constraining the selection of excitation frequencies. A source with two tunable outputs allows the center frequencies to be selected to overlap with peaks of minimum absorptivity (to minimize heating and photodamage) while still maintaining the correct wavenumber difference for CARS imaging.

## 3 Instrumentation

As discussed in Sec. 2, optimal imaging of myelinated tissue requires control of the spectrum of the excitation as well as phase and polarization of the source. A system schematic is shown in Fig 3, with the individual subsystems detailed in the following sections.

### 3.1 Coherent Anti-Stokes Raman Scattering Laser Source

A twin nonlinear optical parametric amplifier (OPA)<sup>15</sup> system pumped by an amplified ytterbium-doped fiber laser (ClarkMXR, Dexter, Michigan) generated both  $\omega_p$  and  $\omega_s$ . Each OPA was tunable from 650 to 1300 nm with an adjustable bandwidth of ~8 to 20 nm. This source satisfied the condition to freely tune both CARS wavelengths to avoid absorption peaks in the sample. The system also provided high-energy pulses at low average power with controllable bandwidths from several nm to over 10 nm.

The outputs of both OPAs were inherently synchronized in phase and repetition rate as the same pump laser drives both. The repetition rate of the OPA system was fixed at 1 MHz (as set by the pump laser) with pulse energies varying from 100 to 200 nJ per pulse. For comparison, a typical titanium sapphire (Ti:Saph) laser system, a common alternative source for nonlinear imaging modalities, typically provides 25 to 50 nJ per pulse at 80-MHz repetition rate. The lower repetition rate of the OPA also reduced average power delivered to the sample, with the OPAs providing 1 nJ per mW average power, whereas

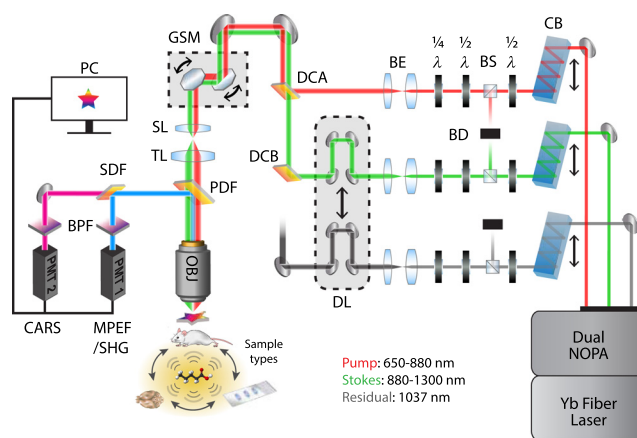


**Fig. 3** Schematic diagram of complete imaging system. From right: Dual NOPA, dual noncollinear optical parametric amplifier; Yb, ytterbium-doped fiber laser (detailed in Sec. 3.1); CB, chirping blocks for dispersion control (Sec. 3.2);  $\frac{1}{2}$  and  $\frac{1}{4}$   $\lambda$ , half- and quarter-waveplates for polarization control (Sec. 3.3); BS, beam splitter; BD, beam dump; BE, beam expander telescope composed of 30- and 100-mm focal-length achromatic lenses; DL, delay line; DCA, dichroic combiner “A” for combining pump and Stokes; DCB, dichroic combiner “B” for permitting optional introduction of the residual beam from the fiber laser; GSM, galvanometer scanning mirror pair; SL, scan lens; TL, tube lens; PDF, primary dichroic filter for separating NIR pump and Stokes beams from visible fluorescence and anti-Stokes signals; SDF, secondary dichroic filter for separating CARS from fluorescence or second harmonic signals; BPF, bandpass filters in interchangeable holders to select desired emission wavelength; and PC, personal computer for acquisition. (Filters and scanning mechanics are detailed in Sec. 3.4.)

a Ti:Saph laser provides a much lower 12.5 pJ per mW of average power (assuming 50 nJ per pulse).

Based on the optical absorption profile of typical lipids,<sup>16</sup> the center wavelengths for  $\omega_p$  and  $\omega_s$  were chosen to be 750 and 963 nm, respectively. This combination allowed Raman interrogation from ~2800 to ~3100  $\text{cm}^{-1}$  with 10- to 20-nm bandwidth (adjustable) in each beam. The center wavelength of the probe at 963 nm is less absorbed by lipid than typical 1040- or 1064-nm laser systems, thus reducing sample heating. The necessary  $\omega_p$  wavelength of 750 nm is not a local minimum; however, it still had an absorption value comparable to 963 nm for lipids.

This frequency versatility, both in center wavelength and bandwidth, allowed the source to be tuned for excitation over the wavenumber span and Raman peak widths of the relevant vibrational features in the lipid region.

### 3.2 Instantaneous Frequency Difference Control Pulse Stretcher

The pulses produced by the OPAs were ~100 fs in duration, approaching the transform limit for their bandwidth. Linear chirp was applied to both pulses to optimize the IFD for the bandwidth of the C–H stretches within the lipid region. A custom prism was designed in-house that propagates a beam through a variable length of glass at normal surface angles for both entrance and exit, manufactured to specification by BMV Optical (Ottawa, Ontario, Canada). Internal metallic silver coatings provided polarization-insensitive internal reflection, whereas the entrance and exit windows feature an antireflection

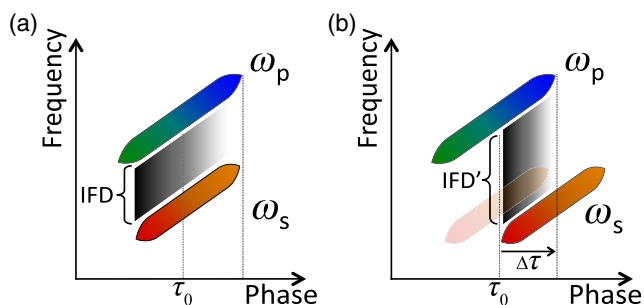


**Fig. 4** (a) Constant IFD between  $\omega_p$  and  $\omega_s$  at  $\tau_0$  and (b) increasing IFD (IFD') by delaying arrival of  $\omega_s$  by time delay  $\Delta\tau$ .

coating optimized for normal incidence and the 650- to 1300-nm wavelength range of the OPAs.

Two blocks were manufactured, one each for  $\omega_p$  and  $\omega_s$ . The path length of each block was adjusted for optimal dispersion for each wavelength. A linear motor delay line (ThorLabs, Newton, New Jersey) in the path of  $\omega_s$  adjusted the arrival time of  $\omega_s$  relative to  $\omega_p$  at the sample, as illustrated in Fig. 4.

### 3.3 Polarization Controller

Polarization control of  $\omega_p$  and  $\omega_s$  at the sample plane was necessary for maximum CARS signal from ordered tissue as discussed in Sec. 2.2. Many optical elements in the microscope induce small polarization artifacts that distort the polarization state of excitation beams. Precompensation of these artifacts was required for delivery of the desired polarization state to the sample plane.

A series of motorized waveplates and a power control system allowed independent polarization control of  $\omega_p$  and  $\omega_s$ . The polarization controllers apply a counter-perturbation on each beam that negates the effects of other optics in the system. A calibration and control system maintained the desired polarization states and equalized sample-plane optical power for all states.

Power normalization is of particular importance for polarization imaging. The optical path of a typical microscope has polarization-sensitive absorption, so different polarization states will exhibit variable power transmission through the optical train. Polarization interrogation of the sample will be artifactually stronger or weaker as the effective power of the lasers at the sample varies with injected polarization.

Calibration and control of polarization and transmitted power were both controlled with custom LabVIEW software (National Instruments, Austin, Texas).<sup>17</sup> The control software suite was capable of generating both linear or specific elliptical polarization states at 5-deg increments for both  $\omega_p$  and  $\omega_s$ . Polarization and power were automatically coordinated with image acquisition through triggered input to the laser-scanning system. The calibration portion of the software measured power and polarization at the sample plane prior to each experiment and used a combination of manual and automatic adjustment to create a state look-up table of waveplate positions prior to imaging.

### 3.4 Microscope Optomechanics and Detection

An open-frame microscope was constructed from bulk parts to minimize the number of optical elements in the design. A Nikon C1 scan head, scan lens, and EZC1 software were used to scan the beams across the sample and manage data acquisition. The

tube lens was a 200-mm focal-length NIR achromatic lens (ThorLabs) and the objective lens was a 25 $\times$  1.1NA CFI75 Apo LWD 25XW (Nikon Instruments, Melville, New York).

A custom 700- or 750-nm primary dichroic (BMV Optical) separates the incident NIR excitation from visible signal. A secondary 585-nm long-pass dichroic (Semrock, Rochester, New York) separated the signal into a red CARS channel and blue/green fluorescence/second harmonic path. A multi-alkali photomultiplier tube (Hamamatsu, Hamamatsu City, Shizuoka Pref., Japan) was used in each detection path.

Polarization of  $\omega_p$  and  $\omega_s$  and the  $\omega_s$  delay line were all controlled by a custom suite of LabVIEW software operating on two PCs. The software allowed synchronized control of image acquisition, excitation wavenumber, and excitation polarization.

## 4 System Characterization

Measurement and calibration of  $\omega_p$  and  $\omega_s$  pulse width and polarization properties were necessary for consistent operation of the instrument. A detailed calibration routine was developed to ensure the consistency of the excitation beams between experiments.

### 4.1 Pulse Chirp and Spectral Measurements

As mentioned previously, the chirp of  $\omega_p$  and  $\omega_s$  impacts the vibrational selectivity of the system. A mixture of microbeads of three different polymers was used as a calibration standard. The polymers, polystyrene (PS), polyethylene (PE), and polymethyl methacrylate (PMMA) are well characterized<sup>18</sup> and have distinctive Raman spectra. The vibrational peaks of these plastics span the range typical for lipid with well-known Raman sensitivity and linewidths. The resolution of the system was determined by measuring a sample of all three plastic beads prior to each experimental session. Any deviation in the bandwidth or location of the peaks would indicate a change in the spectral chirp of  $\omega_p$  and  $\omega_s$ .

The initial chirp required for the system was estimated from the expected bandwidth of the Raman lines in the C–H region. The spectral bandwidth of the pulses was selected to allow tuning of the center Raman vibration spanning  $\sim 2800$  to  $3100\text{ cm}^{-1}$ , comprising most of the lipid region. Tuning was achieved by adjusting the arrival time of  $\omega_p$  and  $\omega_s$  using a delay line in the path of  $\omega_s$ . CARS signal intensity was measured as a function of the delay time, with “0” determined by the maximum resonant signal in a sample of Sylgard 184 Silicone Elastomer (Dow Corning, Auburn, Michigan) offset by  $-700\text{ fs}$  to create a symmetric sweep.

The pulse widths of  $\omega_p$  and  $\omega_s$  were measured using a convolution of the two in a  $10\text{-}\mu\text{m}$ -thick barium borate crystal placed at the sample plane.<sup>19</sup> The delay line was stepped in 200-fs increments while measuring the intensity of the sum frequency generation (SFG) and four-wave mixing (FWM) signals produced in the crystal. The SFG response is dependent on the combination of  $\omega_p$  and  $\omega_s$ , whereas the FWM response is dependent on the square of  $\omega_p$  and linearly with  $\omega_s$ . The difference in dependency between FWM and SFG allows the pulse widths of  $\omega_p$  and  $\omega_s$  to be determined by measuring the pulse widths of the FWM and SFG signals.<sup>20</sup> Using this method, the pulse width of  $\omega_p$  was measured as 6.9 ps, while the pulse width of  $\omega_s$  was measured as 2.7 ps. The FWHM spectral bandwidths of the pulses were measured as 16.9 nm for  $\omega_p$  and 11.5 nm for  $\omega_s$ . Based on the measured spectral bandwidth and pulse widths,

the chirp of  $\omega_p$  was estimated to be 1.29 THz/ps while  $\omega_s$  was 1.38 THz/ps, indicating good chirp matching between both sources.

## 4.2 Polarization Stability

The polarization stability of the system was assessed with a polarimeter (Meadowlark, Frederick, Colorado) prior to every imaging session. The calibration error tolerance was defined as 0.03 elliptic and 1 deg of orientation. These values were determined based on the repeatability of the placement of the polarization measurement apparatus on the microscope stage. The required polarization states were measured at the beginning of each imaging session. Any states outside the tolerance bounds were corrected with small adjustments to the polarization controller before imaging. The updated results were written to the look-up table for the control system.<sup>11</sup>

## 4.3 Excitation Power Stability

The power of both pump and Stokes beams must be normalized at the sample plane to maintain equal excitation over the various applied polarization states. A polarization-insensitive power meter measured the optical power transmitted for each beam at each polarization state. An automated proportional correction algorithm adjusted the input power to the system to compensate for any variation in transmission. This algorithm calibrated the necessary power corrections at each state and saved them back to a look-up table. When a given polarization state was requested, the system would also adjust the power accordingly.

## 5 Results

The performance of the system for myelin imaging was verified by spectral selectivity, feature resolution, and polarization response. A combination of a calibration standard and imaging of peripheral nervous system (PNS) and central nervous system (CNS) myelin was used to examine these three parameters.

### 5.1 Polymer Spectral Calibration

The three polymers, PE, PS, and PMMA, were used to test the spectral selectivity of the chirped pulses. A mixture of

microbeads of the three plastics was immobilized in Sylgard 184 and slide mounted.

The CARS signal intensities shown in Fig. 5 were measured pixel count intensities from an image of the mounted beads. The bead image was acquired in  $\sim 2$  min with delay line steps of 70 fs ( $\sim 3$  cm<sup>-1</sup> per step) providing 101 sample points of spectral data per pixel. The raw data show good agreement with published Raman spectra of the three polymers, with all notable peaks present for the 2800- to 3100-cm<sup>-1</sup> “lipid” region in the Raman/CARS spectra. While a moderate background signal is present, the peaks are all clearly distinguishable without background subtraction or other postprocessing methods. A small false peak is present in the polymer spectra, which is readily identifiable as leak-through from the Sylgard mounting medium [Figs. 5(b) and 5(c)].

### 5.2 Imaging

Fixed dorsal column of wild-type C57BL/6 mouse was imaged to determine the scale of features resolvable by the imaging system in biological samples. The sample was fixed in a solution of 4% paraformaldehyde (PFA) and imaged in 4-(2-hydroxyethyl)-1-piperazineethanesulfonic acid buffer (pH 7).

Images were acquired by sampling 47 discrete delay line steps at 140 fs step size. The resulting CARS spectra were used to generate a false-color image (Fig. 6) by treating the CARS spectra as an equivalent visible light spectrum. ImageTrak software (written by P.K.S.) was used to render the false-color spectral data into a color image. The image showed myelin structure and details from only endogenous CARS signal without additional labeling. Structures corresponding to Schmidt–Lanterman incisures and nodes of Ranvier were clearly visible.

### 5.3 Polarization Response

The directional sensitivity of the system was evaluated by rotating the polarization of  $\omega_p$  and  $\omega_s$  using the polarization controller while acquiring images of CNS and PNS tissue. A dorsal root entry zone (DREZ) junction from mouse spinal cord was a convenient sample for this purpose as it features both CNS and PNS at the same location. The PNS axons are typically arrayed at an angle to the CNS axons as they exit the spinal cord, creating an

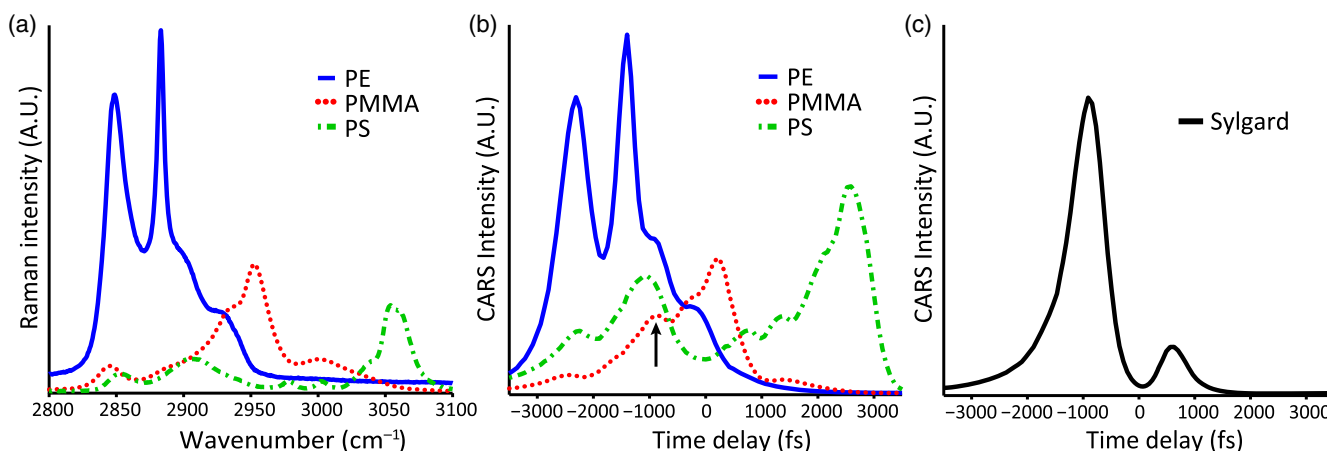


**Fig. 5** (a) Published Raman spectra for PS, PE, and PMMA polymers.<sup>18</sup> (b) Unprocessed CARS spectra acquired from polymer beads mounted in Sylgard 184. Delay axis refers to relative delay in fs between arrival of  $\omega_p$  and  $\omega_s$ . Arrow at  $-700$  fs highlights contamination in the acquired spectra from Sylgard mounting media. (c) Unprocessed CARS spectra of Sylgard showing strong peak at  $-700$  fs.

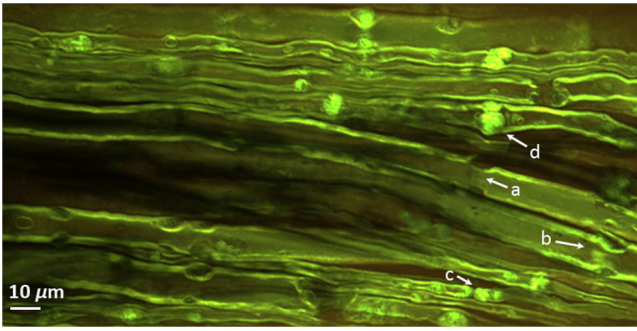


**Fig. 6** False-color CARS image of dorsal column from wild-type mouse fixed with 4% PFA. Arrows denote features of interest including probable (a and b) Schmidt–Lanterman incisures and a (c) node of Ranvier. Submicron features are visible in the axon interiors including (d) small membrane folds and vesicular structures. This image was acquired with excitation polarization aligned with the direction of the axons which maximized signals from normal compacted myelin.

angular difference between two adjacent regions of myelinated tissue.

As expected, the various orientations of myelin in the sample displayed the largest signal when the excitation polarization was aligned parallel to the membrane (Fig. 7). Of particular interest were the small inclusions and nodal gaps in the myelin that are brighter at various angles. In addition, the CARS spectral information of the myelin was found to be polarization dependent. Figure 8 shows the CARS spectra for CNS myelin when the excitation was parallel (0 deg) and orthogonal (90 deg) to the direction of the axons.

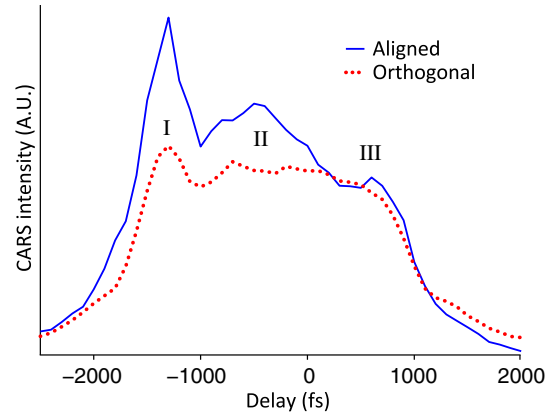


**Fig. 8** CARS spectra of CNS myelin for excitation polarization aligned (solid) and orthogonal (dashed) to the direction of the membrane (longitudinal axons). The three peaks are the  $\text{CH}_2$  symmetric (I),  $\text{CH}_2$  asymmetric (II), and  $\text{CH}_3$  vibrations (III).

## 6 Discussion

### 6.1 Imaging Performance

The system described here provides several advantages over other CARS systems. First, the system makes exciting nonlinear CARS processes more accessible because pulse energies from OPAs used in our configuration are orders of magnitude higher<sup>14</sup> than optical parametric oscillator-based,<sup>2,3,8,20</sup> locked picosecond laser pairs,<sup>7,12</sup> or super-continuum generation systems<sup>1</sup>

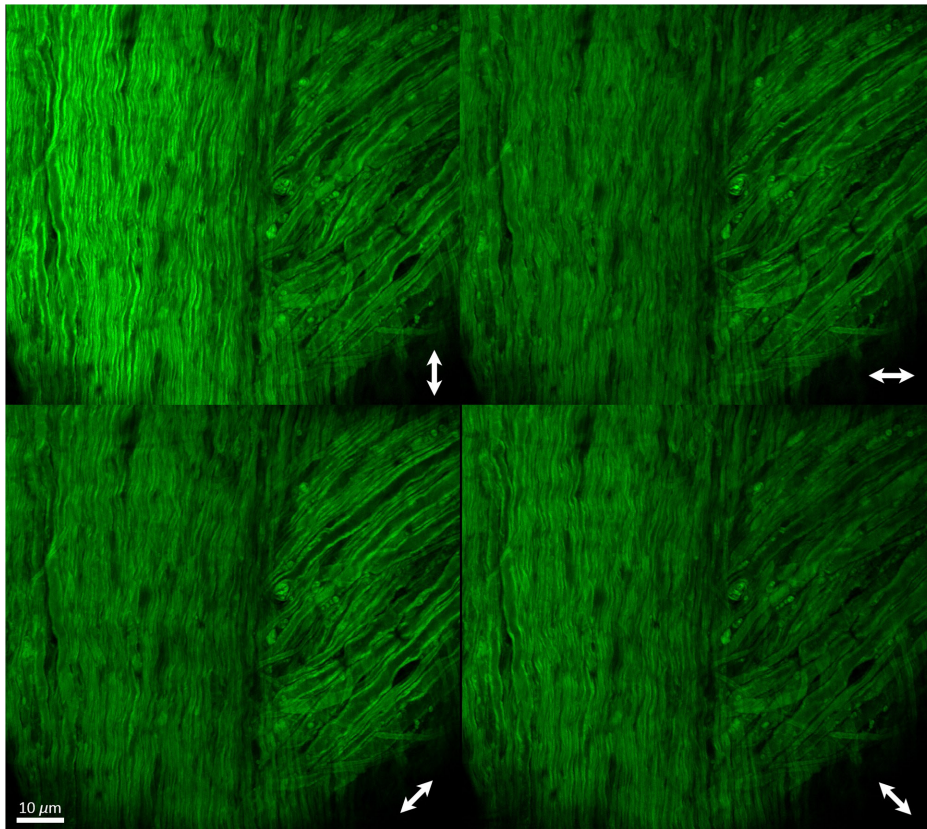


**Fig. 7** DREZ of wild-type mouse spinal column (dorsal) imaged with polarized CARS excitation. Double-headed arrows indicate direction of linearly polarized  $\omega_p$  and  $\omega_s$  for each image.

typically used for CARS imaging. The OPAs used in this work produced >100 nJ per pulse compared to <10 nJ typical of non-OPA systems. This means that even after chirping, sufficient peak energy remains for the pump and Stokes pulses to efficiently drive the nonlinear CARS process. The low pulse energy of Ti:Saph laser and parametric oscillator systems does not provide sufficient initial peak energy to tolerate high temporal chirp without compromising peak-energy-dependent CARS signal generation.

In comparison, the 3- to 7-ps-duration outputs derived from the femtosecond high-energy OPA pair can be stretched to meet vibrational bandwidth requirements while still producing CARS signal. This is emphasized in the low background signal and high resolution exhibited by the polymer test samples in Sec. 5.1, compared against a standard Raman spectrometer. Note that the CARS spectrum of the plastic samples was acquired with no averaging, highlighting the effectiveness of the energetic chirped pulses.

Another advantage is that the high-energy twin OPA sources used for both the pump and Stokes can acquire an image in a single frame pass, without the need for averaging of multiple frames. Note that the pixel dwell in all acquired images was 2 to 3  $\mu$ s, which is on par with standard confocal and multiphoton microscopy.<sup>8,9</sup> Each pixel in the image received only 2 or 3 laser pulses, based on the 1-MHz repetition rate of the OPAs.

The pulse width and wavelength flexibility of the dual-OPA system are also useful for multimodal imaging complementary to CARS. Depending on the needs of the experiment, the system allows the researcher to control the pulse width and thus optimize the imaging performance of nonlinear imaging, such as multiphoton fluorescence or second harmonic generation, while retaining tuning flexibility of the second output to select a wavelength optimal for CARS.

## 6.2 Bond Directionality

From the spectral information in Fig. 8, it is notable that the CH<sub>2</sub> bond (peak I) exhibits the greatest sensitivity to polarization. This is not unexpected, because in lipid chains these bonds are highly organized and directional. Conversely, CH<sub>3</sub> bonds tend to exist at the terminus of the acyl chains and are less constrained in orientation. While CH<sub>2</sub> bonds do exist in other molecules in the membrane that lack orientation, the dense packing and organization of lipid cause the CH<sub>2</sub> signal to dominate when the excitation fields are aligned with these bonds. Intriguingly, small folds, vesicles, and membrane structures are emphasized at specific polarization states for the CH<sub>2</sub> resonance. Many of these features appear to be located inside the axons, illustrating the ability to image structures that fluorescent markers may be unable to reach.

The polarization selectivity of the system, combined with the rapid wavenumber tunability of the source, allows the directionally sensitive CH<sub>2</sub> vibration to be compared to the less-sensitive CH<sub>3</sub> resonance. This provides simultaneous orientational and compositional information for each pixel in an image. The polarization controllers also permit image acquisition at specific polarization states during an image series, allowing faster imaging of only a few states, or longer imaging of many states as the situation requires. Compared to freely rotating polarization CARS systems,<sup>1</sup> this permits more selective control over sample exposure by only exposing the sample to the lasers for the desired polarization orientations. For instance sparse sampling can be performed with the system tuned to the polarization-

insensitive CH<sub>3</sub> vibration, whereas more polarization states may be sampled for the directionally sensitive CH<sub>2</sub> vibrations.

## 7 Conclusions

The combination of high-energy pulses, matched frequency chirp, and polarization control has permitted the acquisition of very detailed myelin images. Spectral and orientational information were acquired in combination with fine structural detail through careful control of these excitation parameters. Custom dispersing prisms combined with high pulse energy allowed a high degree of chirp while maintaining sufficient pulse energy for strong nonlinear CARS signal without sacrificing chemical specificity.

CARS spectral resolution was found to be comparable to spontaneous Raman spectra of common plastic calibration standards. The system was able to discern the Raman-active peaks between 2800 and 3100  $\text{cm}^{-1}$  with reasonable approximation of the relative intensities of each peak. These features were resolved with detail approaching published spontaneous Raman spectra without the need for postprocessing.

The control of excitation polarization combined with fine Raman spectral resolution provided insight into the orientation of the dominant CARS vibrations within a sample. Altering polarization also highlighted specific features within a complex multidirectional DREZ sample. Fine features within mouse dorsal column were apparent with good contrast against the background.

In future work, the system will allow the investigation of myelin orientational information for a variety of injury and disease models. The acquisition of polarization data will allow exploration of the molecular organization of C–H vibrations under these conditions in fixed and living samples of myelinated tissue, in turn informing on nanostructural integrity of myelin sheaths that can only be obtained with technically difficult methods, such as x-ray diffraction, that do not provide two-dimensional images of the sample. The vibrational specificity of the system will also allow the exploration of the difference between more and less directionally sensitive vibrational modes and their orientations. Observing the positioning, concentration, and evolution of these vibrational modes may shed light on the mechanisms of disorder and breakdown in these samples, in which membrane order is essential for proper physiological function.

## Disclosures

The authors declare that there are no conflicts of interest related to this article.

## Acknowledgments

This work was made possible by funding from the Canada Research Chairs, the Canadian Institutes for Health Research, the Canada Foundation for Innovation, and the Alberta Innovates–Health Solutions Collaborative Research and Innovation Opportunities grant to P.K.S., and the Multiple Sclerosis Society of Canada EndMS Doctoral Studentship Award to Craig Brideau.

## References

1. G. de Vito et al., “RP-CARS: label-free optical readout of the myelin intrinsic healthiness,” *Opt. Express* **22**(11), 13733–13743 (2014).

2. C. Cleff et al., "Direct imaging of molecular symmetry by coherent anti-Stokes Raman scattering," *Nat. Commun.* **7**, 11562 (2016).
3. P. Gasecka et al., "Lipid order degradation in autoimmune demyelination probed by polarized coherent Raman microscopy," *Biophys. J.* **113**(7), 1520–1530 (2017).
4. G. Eckhardt, D. P. Bortfeld, and M. Geller, "Stimulated emission of Stokes and anti-Stokes Raman lines from diamond, calcite, and  $\alpha$ -sulfur single crystals," *Appl. Phys. Lett.* **3**(8), 137–138 (1963).
5. W. M. Tolles et al., "A review of the theory and application of coherent anti-Stokes Raman spectroscopy (CARS)," *Appl. Spectrosc.* **31**(4), 253–271 (2016).
6. P. D. Maker and R. W. Terhune, "Study of optical effects due to an induced polarization third order in the electric field strength," *Phys. Rev.* **137**(3A), A801–A818 (1965).
7. H. Wang et al., "Coherent anti-Stokes Raman scattering imaging of axonal myelin in live spinal tissues," *Biophys. J.* **89**(1), 581–591 (2005).
8. C. L. Evans and X. S. Xie, "Coherent anti-Stokes Raman scattering microscopy: chemical imaging for biology and medicine," *Annu. Rev. Anal. Chem.* **1**(1), 883–909 (2008).
9. A. Alfonso-García et al., "Biological imaging with coherent Raman scattering microscopy: a tutorial," *J. Biomed. Opt.* **19**(7), 071407 (2014).
10. K.-A. Nave and H. B. Werner, "Myelination of the nervous system: mechanisms and functions," *Annu. Rev. Cell Dev. Biol.* **30**(1), 503–533 (2014).
11. G. Cerumenati et al., "Lipids in the nervous system: from biochemistry and molecular biology to patho-physiology," *Biochim. Biophys. Acta, Mol. Cell. Biol. Lipids* **1851**(1), 51–60 (2015).
12. A. P. Kennedy, J. Sutcliffe, and J.-X. Cheng, "Molecular composition and orientation in myelin figures characterized by coherent anti-Stokes Raman scattering microscopy," *Langmuir* **21**(14), 6478–6486 (2005).
13. C. Lee and C. D. Bain, "Raman spectra of planar supported lipid bilayers," *Biochim. Biophys. Acta, Biomembr.* **1711**(1), 59–71 (2005).
14. K. P. Knutsen et al., "Chirped coherent anti-Stokes Raman scattering for high spectral resolution spectroscopy and chemically selective imaging," *J. Phys. Chem. B* **110**(12), 5854–5864 (2006).
15. C. Brideau, K. Poon, and P. K. Stys, "Broadly tunable high-energy spectrally focused CARS microscopy with chemical specificity and high resolution for biological samples," *SPIE Proc.* **8588**, 85880E (2013).
16. R. L. P. van Veen et al., "Determination of visible near-IR absorption coefficients of mammalian fat using time- and spatially resolved diffuse reflectance and transmission spectroscopy," *J. Biomed. Opt.* **10**(5), 054004 (2005).
17. C. Brideau and P. K. Stys, "Automated control of optical polarization for nonlinear microscopy," *SPIE Proc.* **8226**, 82263A (2012).
18. J. L. Koenig, *Infrared and Raman Spectroscopy of Polymers*, Smithers Rapra Publishing, Shropshire, United Kingdom (2001).
19. W. Liu, L. Zhu, and C. Fang, "Observation of sum-frequency-generation-induced cascaded four-wave mixing using two crossing femtosecond laser pulses in a 0.1 mm beta-barium-borate crystal," *Opt. Lett.* **37**(18), 3783–3785 (2012).
20. V. Piazza et al., "Femtosecond-laser-pulse characterization and optimization for CARS microscopy," *PLoS One* **11**(5), e0156371 (2016).

**Craig Brideau** is an engineering scientist at the University of Calgary. He received his MASC degree in electrical engineering from Dalhousie University in 2007 and his PhD in biomedical engineering from the University of Calgary in 2018. His current research interests include nonlinear optical imaging, spectroscopy, and automation. He is a well-known contributor to the confocal microscopy list server hosted by the University of Minnesota.

**Kelvin W. C. Poon** received his masters in forensic science and PhD in analytical chemistry from the University of Western Australia with postdoctoral fellowships at Dublin Institute of Technology and the University of Calgary. He has extensive experience in biomedical optics, advanced microscopy, imaging, analytical chemistry, spectroscopy and tissue pathology. Currently, he is a Research Analyst/Imaging Specialist at the University of Calgary's Hotchkiss Brain Institute Advanced Microscopy Platform core facility.

**Pina Colarusso** directs the Live Cell Imaging Laboratory (LCI) at the University of Calgary. Pina has a PhD in chemistry from the University of Waterloo and is an experienced microscopist who collaborates with and supports researchers across disciplines. She helps foster the adoption and development of emerging technology and quantitative analysis in her local research community. She also spearheaded development of the educational program in optical microscopy, which emphasizes learner-centered, experiential opportunities.

**Peter K. Stys** is an MD, clinical neurologist, and researcher. He has devoted the majority of his research career to the study of myelinated axons, with major relevance to prevalent disorders such as stroke, MS and spinal cord injury. A large portion of his current work is aimed at understanding the degenerative mechanisms underlying MS, using advanced techniques such as spectral confocal microscopy, polarization-dependent 2-photon microscopy and spectral coherent anti-Stokes Raman scattering microscopy (sCARS).